3.1. Introduction

As discussed in Chapter 1, manganites with perovskite structure are intensively investigated due to the property of colossal magnetoresistance (CMR) and its potential applications in the field of technology, magnetic memory and solid oxide fuel cells [Ramirez (1997); Wang et al. (2000); Hu et al. (2014)]. In recent years, most attention was given to nano-sized mixed valence perovskite manganites $R_{1-x}A_xMnO_3$, where R and A are rare earth and alkaline earth elements respectively because they exhibit interesting properties which do not appear in the bulk systems, like appearance of Griffiths' phase, exchange bias effect, and suppression of charge ordering [Markovich et al. (2014); Dayal et al. (2014); Giri et al. (2014a); Shankar et al. (2015)]. The $Nd_{0.7}Ba_{0.3}MnO_3$ manganite belongs to a family of Ba^{2+} substituted neodymium manganites with CMR properties [Wang et al. (2000); Roy et al. (2008)]. The replacement of trivalent Nd^{3+} ions by divalent Ba^{2+} ions in the stoichiometric $NdMnO_3$ parent compound leads to the formation of mixed valence perovskite manganite [Wang et al. (2000); Roy et al. (2008); Wu et al. (2000)].

As discussed in Chapter 1, effect of Ti-substitution at Mn-site has been studied in several perovskite manganites. Jemaa et al. (2015) reported the structural, magnetic, magnetocaloric (MC) and critical behavior of Ti-doped $La_{0.67}Ba_{0.22}Sr_{0.11}Mn_{1-x}Ti_xO_3$ and observed that the replacement of Mn by Ti increased the unit cell volume and significant shift in T_C towards lower temperature values on the increasing Ti-component up to $x \leq 0.2$ due to weakening of DE ferromagnetic coupling. Kulkarni et al. (2008) investigated the structural, magnetic, transport and spectroscopic properties of Ti-doped $La_{0.67}Sr_{0.33}MnO_3$, and found that the substitution of Mn by Ti decreased the hybridization between O_{2p} and Mn_{3d} ions and the bandwidth, leading to the shift of the T_C towards lower value on increasing Ti concentration. Gasmi et al. (2009) also studied

the effect of the Ti-doping on the structural and magnetic properties of $La_{0.67}Ba_{0.33}Mn_{1-x}Ti_xO_3$ and found a decrease of the T_C in the compounds with $x \leq 0.1$ on increasing Ti-doping concentration. At the same time, samples with $x \geq 0.2$ illustrated spin-glass (SG) like behaviors. Similar kind of significant investigation for Ti-doping has been studied in $La_{0.7}Sr_{0.3}Mn_{1-x}Ti_xO_3$ [Phong et al. (2016a)], $La_{0.5}Sr_{0.5}Mn_{1-x}Ti_xO_3$ [Shang et al. (2014)], $LaMn_{1-x}Ti_xO_3$ [Yang et al. (2005)], $La_{0.4}Bi_{0.6}Mn_{1-x}Ti_xO_3$ [Dayal et al. (2015)] and $La_{0.7}Ca_{0.3}Mn_{1-x}Ti_xO_3$ [Zhu et al. (2010)].

Zhu et al. (2006) studied structural, magnetic and transport properties of Ti-doped $La_{0.7}Sr_{0.3}Mn_{1-x}Ti_xO_3$ ($0 \leq x \leq 0.5$) thin films and observed that for $x \leq 0.3$, Ti^{4+} ions replace Mn^{4+} ions resulting expansion in lattice while for $x > 0.3$ Ti^{4+} substitute Mn^{3+} ions causing lattice contraction. They also noticed that T_C decreases with the increase of Ti^{4+} ions doping content. Recently, Ho et al. (2016) investigated the influence of Ti doping on critical behavior and magnetocaloric effect of $La_{0.7}Ba_{0.3}Mn_{1-x}Ti_xO_3$ with $x = 0.05$ & 0.10 and found that the magnetic phase transition falls into 3D Heisenberg and 3D Ising universality classes, respectively. The theoretical values of critical exponents β, γ and δ for ideal short-range magnetic interaction as per 3D Heisenberg model is 0.365, 1.336 and 4.800, respectively, on the other hand, the theoretical values of critical exponents β, γ and δ for ideal 3D Ising model comes to be 0.325, 1.241 and 4.820, respectively [Jemma et al. (2015); Ho et al. (2016); Zhu et al. (2010); Dayal et al. (2015); Chaikin et al. (2000); Baazaoui et al. (2016)]. While, as per theoretical mean-field model for long-range interaction, the critical exponents β, γ and δ have ideal values of 0.5, 1.0 and 3.0, respectively [Dayal et al. (2015); Amaral et al. (2004)]. In this study, we have selected $Nd_{0.7}Ba_{0.3}Mn_{1-x}Ti_xO_3$ (NBMTO) ceramics to explore the structural and magnetic properties due to the following reasons: (i) to the best of our knowledge effect of Ti-substitution on the properties of $Nd_{0.7}Ba_{0.3}MnO_3$ have not been studied so far (ii) it

is expected that Ti^{4+} will substitute Mn^{4+} ions, which may strongly influence the crystal structure, bond lengths and angles, and nature of magnetic interactions (iii) it has been recognized in $La_{0.7}Ca_{0.3}Mn_{1-x}Ti_xO_3$ manganites that decrease in the rate of T_C due to Ti-doping is very sharp for low Ti-doping content, while for higher Ti-doping content it flattens [Zhu et al. (2010)], it will be interesting to know how it varies in the present system (iv) it has been identified that Ti-doped manganites show first-order magnetic transition, which may be a better candidate for refrigeration application in magnetic cooling. Phan et al. (2015) reported that Y-doped $La_{0.7-x}Y_xCa_{0.3}MnO_3$ ($0 \leq x \leq 0.08$) manganites exhibit first-order magnetic transition (FOMT) for $x \geq 0.06$ and second-order magnetic transition (SOMT) for $x = 0.08$. They observed that maximum change in magnetic-entropy varies from 10.7 $J.Kg^{-1}.K^{-1}$ for the sample having FOMT ($x = 0$) to 5.8 $J.Kg^{-1}.K^{-1}$ for the sample having SOMT ($x = 0.08$). These results show that the samples exhibiting FOMT are more suitable for the application in magnetic refrigeration. Motivated by these aspects, we investigated polycrystalline samples of $Nd_{0.7}Ba_{0.3}Mn_{1-x}Ti_xO_3$, to determine the nature and order of magnetic phase transition. Doping of Ti^{4+}-ion at the Mn-site is also found to be very effective in tuning the magnetic phase transition temperature which can be important of magnetocaloric cooling in the different temperature range.

In this chapter, we have studied the effect of Ti-doping on structural transformation using X-ray diffraction (XRD) patterns as well as the magnetic phase transition of polycrystalline $Nd_{0.7}Ba_{0.3}Mn_{1-x}Ti_xO_3$ ($0 \leq x \leq 0.30$) (NBMTO) manganites. The crystallographic structural analysis was performed by Rietveld refinement of XRD patterns. However, the detailed study about magnetic properties was carried out by temperature and field dependent magnetizations and frequency dependent ac susceptibility measurements.

3.2. Experimental Details

The polycrystalline samples of $Nd_{0.7}Ba_{0.3}Mn_{1-x}Ti_xO_3$ ($0 \leq x \leq 0.30$) perovskite manganites were synthesized by using an auto-combustion process of the chemical route. The details of the synthesis of the $Nd_{0.7}Ba_{0.3}Mn_{1-x}Ti_xO_3$ manganites samples are given in Chapter 2. The obtained blackish powder during the synthesis process was collected. Then obtained brownish-black powder was grinded. First of all, the grinded powder of $Nd_{0.7}Ba_{0.3}Mn_{1-x}Ti_xO_3$ with $x = 0$ was calcined at different temperatures to optimize the calcination temperature to get the pure phase of the sample. It was found that the sample $Nd_{0.7}Ba_{0.3}MnO_3$ calcined at 1200°C for 6 hrs appearances in a pure phase and the details of the experiments are reported in the ref. [Kumar et al. (2018b)]. After the optimization of calcination temperature, other samples were calcined at 1200°C for 6 hrs in a programmable muffle furnace and allowed to cool down to room temperature in the oxygen atmosphere to form pure phase. The X-ray diffraction (XRD) patterns of calcined powders were recorded in 2θ range 20°-120° using Rigaku Miniflex diffractometer with Cu-target. The crystal structure of the samples was analyzed by Rietveld refinement using FullProf Suite [Carvajal (1993)]. For modeling XRD patterns, we considered Pseudo-Voigt function for peaks profiles while the background was modeled using six coefficients polynomial function. Microstructural and elemental analyses were performed by scanning electron microscopy (SEM) and energy dispersive X-ray spectroscopy (EDS) measurements, respectively, using Zeiss Evo 18 Research system. The magnetic characterization of the samples has been done by using Quantum Design, superconducting quantum interference device (SQUID), Magnetic Property Measurement System (MPMS-3) vibrating sample magnetometer (VSM). The temperature dependent magnetization M(T) in the temperature range 2 K $\leq$ T $\leq$ 300 K were measured under zero field cooled (ZFC) and field-cooled (FC) conditions at a

constant applied field of H = 200 Oe for x = 0.0, 0.10, 0.20 & 0.30 and H = 250 Oe for

x = 0.05, 0.15 & 0.25. The field dependence of magnetization M(H) up to ± 60 kOe

were measured at 10 K for x = 0.0, 0.10, 0.20 & 0.30 and up to ± 50 kOe for x = 0.05,

0.15 & 0.25 at 5 and 50 K. The temperature dependence of ac-susceptibility $\chi_{ac}(T)$ in the

temperature between 2 K ≤ T ≤ 300 K were measured at two different frequencies of

100 and 700 Hz for x = 0.0, 0.10, 0.20 & 0.30.

3.3.   Results and Discussion

3.3.1. Microstructural and Elemental Analysis

The powder samples of $Nd_{0.7}Ba_{0.3}Mn_{1-x}Ti_xO_3$ with x = 0, 0.05, 0.10, 0.15, 0.20,

0.25 and 0.30 were examined by scanning electron microscopy (SEM) to determine the

grain morphology and grain size. **Figs. 3.1**(a-g) show representative micrographs of the

samples under examination. The first observation of the micrographs shows that the

variation in the composition of the samples causes significant morphological changes in

grain size. The average particle size (d_{SEM}) was determined from the SEM micrographs

using ImageJ software by considering as many particles as possible. The calculated

average grain size for x = 0, 0.05, 0.10, 0.15, 0.20, 0.25 and 0.30 was found to be 375,

460, 545, 555, 565, 650 and 435 nm, respectively. The crystallite size for all the

samples was determined using the Scherrer formula, $d_x = 0.89\lambda/\beta_s\cos\theta_B$, where λ is

the wavelength of the radiation used for XRD measurement, β_s is FWHM of the highest

intensity peak after subtraction of instrumental broadening and θ_B is corresponding

Bragg's angle. The crystallite sizes calculated from XRD are found to be 46.01, 68.78,

53.42, 47.41, 46.27, 52.85 and 39.41 nm for x = 0, 0.05, 0.10, 0.15, 0.20, 0.25 and 0.30,

respectively, which are much smaller than the average grain size obtained from SEM

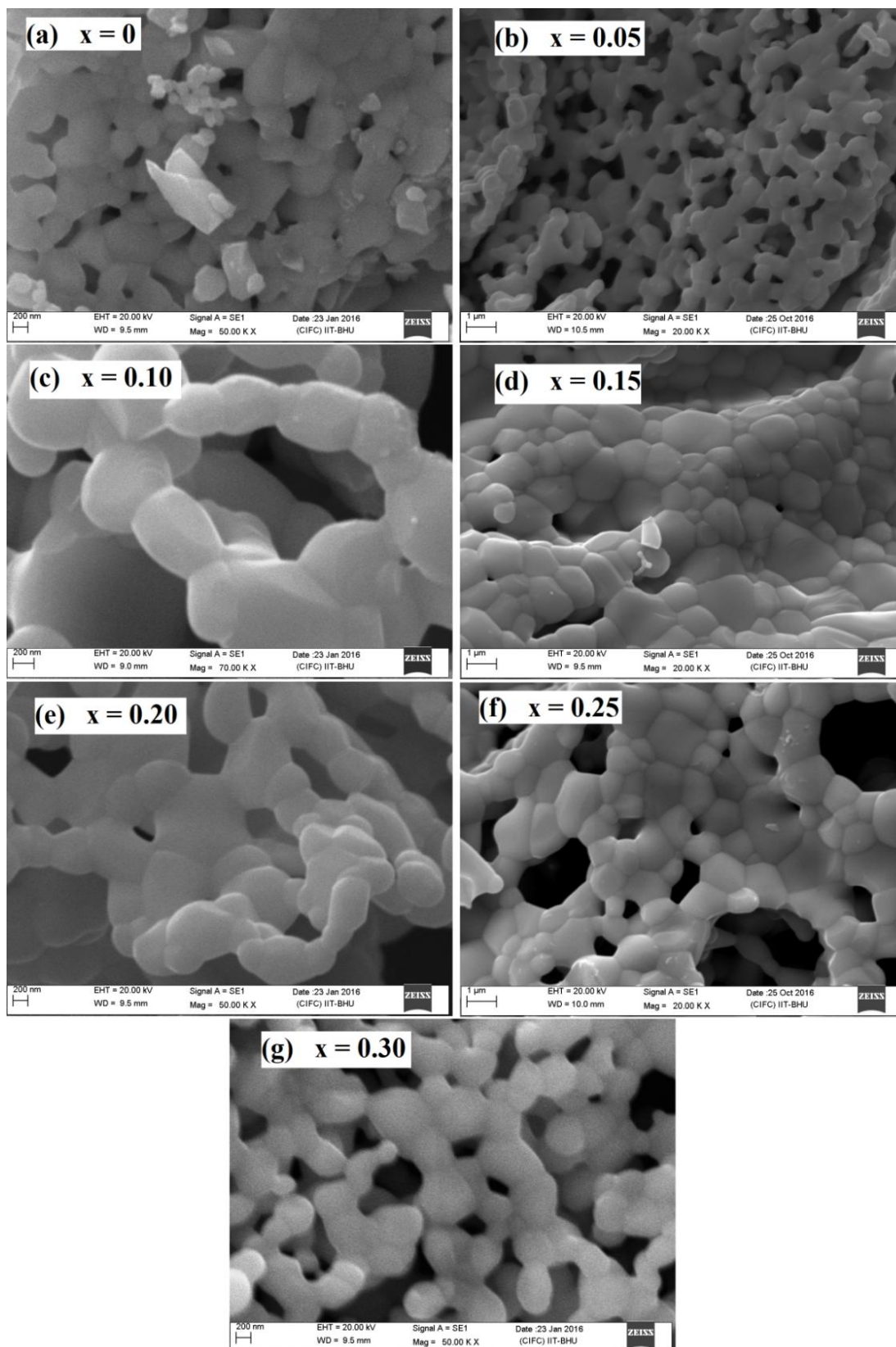micrographs. This implies that grains are made of several crystallites.

Figure 3.1: The scanning electron microscopic (SEM) images of $Nd_{0.7}Ba_{0.3}Mn_{1-x}Ti_xO_3$ perovskite manganites for (a) x = 0, (b) x = 0.05, (c) x = 0.10, (d) x = 0.15, (e) x = 0.20, (f) x = 0.25 and (e) x = 0.30.

The nominal composition of each sample was studied by energy dispersive X-ray spectroscopy (EDS) measurement equipped in the scanning electron microscope. The quantitative elemental analysis was performed without quantifying oxygen, a lighter element, as this technique of elemental analysis is not suitable for quantitative elemental analysis for lighter elements. Thus, we only considered these results for qualitative analysis to identify the elements present in the samples rather than accurate quantitative analysis. The EDS spectra of the three samples are shown in **Figs. 3.2**(a-g). In these spectra, the characteristic peaks of Nd, Ba, Mn, Ti, and O clearly show the existence of all the chemical elements as introduced in the starting powder samples. The atomic percentages of elements experimentally observed from EDS and theoretically calculated for the nominal compositions of $Nd_{0.7}Ba_{0.3}Mn_{1-x}Ti_xO_3$ perovskite manganites with x = 0, 0.05, 0.10, 0.15, 0.20, 0.25 and 0.30 are given in **Table 3.1**. The observed and calculated values of atomic percentages are very close to each other within the expected experimental error. **Table 3.1** clearly shows that with increasing doping concentration of Ti^{4+}-ions at Mn-site, the atomic percentages of Mn atom decreases and Ti-atom increases as per the nominal compositions.
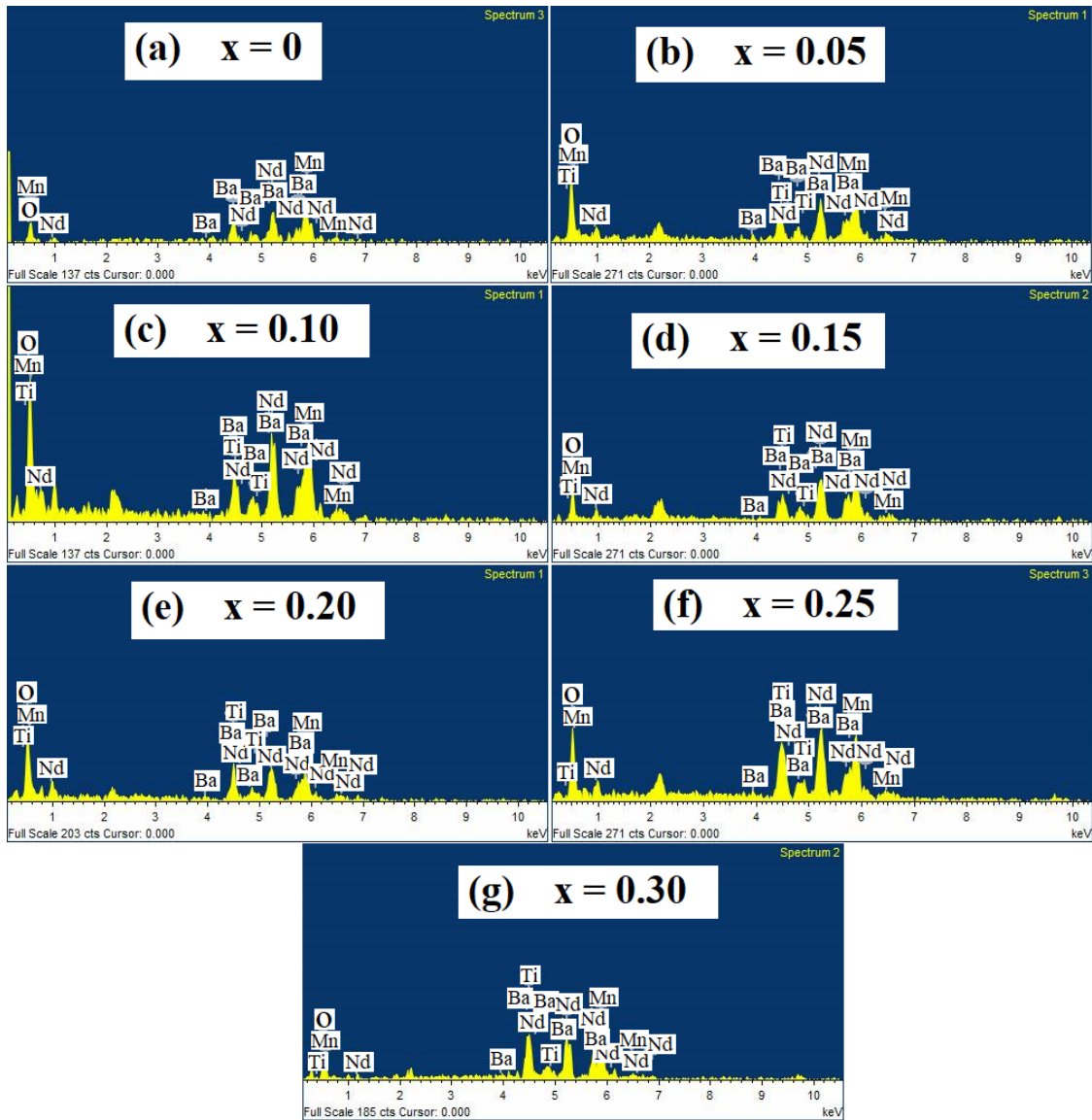
Figure 3.2: The energy dispersive X-ray spectroscopy (EDS) spectra of $Nd_{0.7}Ba_{0.3}Mn_{1-x}Ti_xO_3$ manganites for (a) x = 0, (b) x = 0.05, (c) x = 0.10, (d) x = 0.15, (e) x = 0.20, (f) x = 0.25 and (e) x = 0.30.

Table 3.1: Experimentally observed and theoretically calculated atomic percentages for the Nd, Ba, Mn and Ti atoms present in $Nd_{0.7}Ba_{0.3}Mn_{1-x}Ti_xO_3$ ($0 \leq x \leq 0.30$) perovskite manganites obtained from EDS measurements.

x	Nd		Ba		Mn		Ti	
	Theo.	**Exp.**	**Theo.**	**Exp.**	**Theo.**	**Exp.**	**Theo.**	**Exp.**
0	35.00	32.61	15.00	19.06	50.00	48.33	0.00	0.00
0.05	35.00	30.96	15.00	18.37	47.50	49.64	2.50	1.03
0.10	35.00	35.74	15.00	12.62	45.00	45.50	5.00	6.17
0.15	35.00	37.17	15.00	11.77	42.50	43.28	7.50	7.77
0.20	35.00	32.38	15.00	19.58	40.00	38.72	10.00	9.32
0.25	35.00	32.52	15.00	14.71	37.50	41.09	12.50	11.68
0.30	35.00	33.54	15.00	20.95	35.00	30.93	15.00	14.59

3.3.2. Structural Analysis: Rietveld Refinement

Fig. 3.3 demonstrates the room temperature XRD patterns for $Nd_{0.7}Ba_{0.3}Mn_{1-x}Ti_xO_3$ perovskite manganites with x = 0, 0.05, 0.10, 0.15, 0.20, 0.25 and 0.30 prepared at 1200^oC calcination temperature. No, any impurity phase was detected in the XRD patterns of the samples with x = 0, 0.10, 0.20 and 0.30. A very small (less than 2%) impurity phase of Mn_3O_4 is detected for the samples with x = 0.05, 0.15 and 0.25 due to insoluble Mn_3O_4 having strongest XRD peak at $2\theta = 36.2°$. Further, the shape of the peak for the sample with x = 0.30 is different from the other samples, which suggests a different structure or the coexistence of two different crystallographic phases. As confirmed from Rietveld structure refinement there is coexistence of two different crystallographic phases for x = 0.30. The XRD pattern of parent sample (x = 0) can be indexed using a single phase of the orthorhombic crystal structure with *Imma* space group [Roy et al. (2008)]. Similar to the parent sample, other samples with $0.05 \leq x \leq 0.25$ can also be indexed by a single orthorhombic phase, this shows that there is no

structural phase transition on doping of Ti^{4+}-ions up to x = 0.25. However, the XRD for the sample with x = 0.30 can be indexed considering two crystallographic phases of tetragonal structure with *I4/mcm* and *P4mm* space groups, which indicates a structural phase transition close to x ~ 0.30. Thus, the Rietveld refinement of XRD patterns for $0 \leq x \leq 0.25$ has been performed considering body-centered orthorhombic *Imma* space group and for the sample x = 0.30 using two phases *I4/mcm* and *P4mm*. During the process of Rietveld analysis, we consider the substitution of Ti^{4+} ions at Mn-site. In the orthorhombic crystal structure with *Imma* space group, Nd^{3+}/Ba^{2+} ions occupy 4(e)-site at (0, 0.25, δz), $Ti^{4+}/Mn^{4+}/Mn^{3+}$ ions occupy 4(b)-site at (0, 0, 0.5), $O^{2-}(1)$ ions occupy 4(e)-site at (0, 0.25, δz) and $O^{2-}(2)$ ions occupy the 8(e)-site at (0.75, δy, 0.25), while, in the tetragonal crystal structure with *P4mm* space group, Nd^{3+}/Ba^{2+} ions occupy 1(a)-site at (0, 0, 0), $Ti^{4+}/Mn^{4+}/Mn^{3+}$ ions substitute 1(b)-site at (0.5, 0.5, δz), $O^{2-}(1)$ ions occupy 2(c)-site at (0.5, 0, δz) and $O^{2-}(2)$ ions occupy the 2(c)-site at (0, 0.5, δz). In tetragonal structure with *I4/mcm* space group, Nd^{3+}/Ba^{2+} ions occupy 4(b)-site at (0.5, 0, 0.25), $Ti^{4+}/Mn^{4+}/Mn^{3+}$ ions occupy 4(c)-site at (0, 0, 0), $O^{2-}(1)$ ions occupy 4(a)-site at (0, 0, 0.25) and $O^{2-}(2)$ ions occupy the 8(h)-site at (δx, δy, 0). The detailed results for various parameters obtained from Rietveld structure refinements are given in **Table 3.2**.
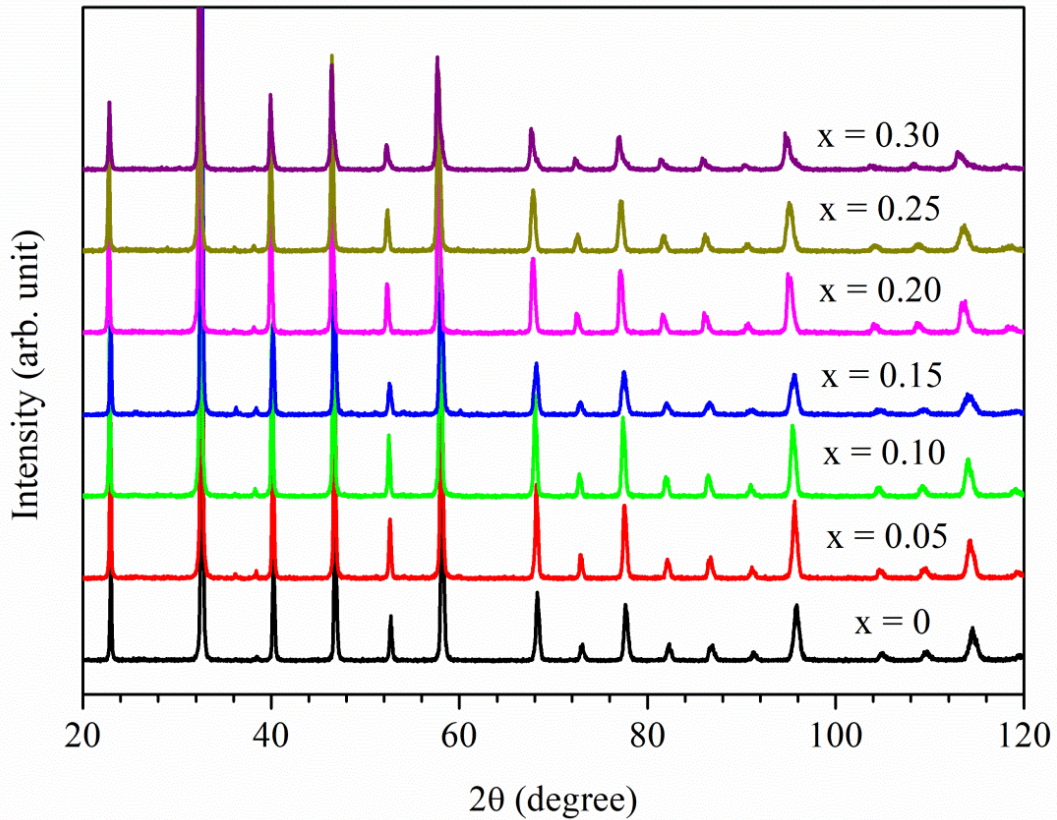
Figure 3.3: Room temperature X-ray diffraction patterns of $Nd_{0.7}Ba_{0.3}Mn_{1-x}Ti_xO_3$ for x = 0, 0.05, 0.10, 0.15, 0.20, 0.25 and 0.30.

Fig. 3.4 shows the Rietveld fits for the XRD patterns of $Nd_{0.7}Ba_{0.3}Mn_{1-x}Ti_xO_3$ manganites with x = 0, 0.05, 0.10, 0.15, 0.20, 0.25 and 0.30. Dots indicate the experimental XRD data and the calculated data is the continuous line overlapping them. The lowest curve shows the difference between experimental and calculated XRD patterns. The vertical bars indicate the expected Bragg's reflection positions. In **Fig. 3.4**(g) upper vertical bars indicate the Bragg's position for *P4mm*, while the lower vertical bars for *I4/mcm* space groups. The lattice parameters of the parent compound (x = 0), a = 5.4908(8) Å, b = 7.7694(9) Å, and c = 5.5109(7) Å are found to be comparable to earlier reported values [Wang et al. (2000); Roy et al. (2008)]. The obtained values of lattice constants and unit cell volume are listed in **Table 3.2**. They exhibit that the

lattice parameters and unit cell volume of the $Nd_{0.7}Ba_{0.3}Mn_{1-x}Ti_xO_3$ samples increase monotonically with enhancing doping concentration of Ti^{4+}-ion. This is due to replacement of small size Mn^{4+} cations (r_{Mn}^{4+} = 0.530 Å) by larger size Ti^{4+} cations (r_{Ti}^{4+} = 0.605 Å) as reported in other Ti-doped manganite systems also [Jemma et al. (2015); Gasmi et al. (2009); Radaelli et al. (1997b)]. The average values of the Mn-O-Mn bond angle ($\theta_{Mn-O-Mn}$) and bond lengths $<d_{Mn-O}>$ for the $Nd_{0.7}Ba_{0.3}Mn_{1-x}Ti_xO_3$ manganites were estimated using results of CIF (crystallographic information file) files generated during Rietveld structure refinement.

The unit cell volume of the distorted perovskite structures can be given by the Equation (3.1):

$$V_{dis} \approx Z\left[2 < d_{Mn-O} > \cos \frac{1}{2}(\pi - \gamma)\right]^3 \qquad (3.1)$$

Where, Z is the number of formula units present per unit cell (here, Z = 4 for *Imma* and *I4/mcm* space groups and Z = 1 for *P4mm* space group), $<d_{Mn-O}>$ is average bond length between Mn and O, $\gamma = <\theta_{Mn-O-Mn}>$ average bond angle between Mn-O-Mn [Radaelli et al. (1997b)]. It is notable that the behaviors of $<d_{Mn-O}>$ and of $<\theta_{Mn-O-Mn}>$ have opposite effects on the unit cell volume. The estimated unit cell volume using the above equation is listed in **Table 3.2** and found to be in good agreement with the values obtained from Rietveld structure refinement. The slight mismatch between the two values of the unit cell results from the distortion of the perovskite structure. For the ideal cubic perovskite structure the values of the unit cells determined from the two methods will be the same.

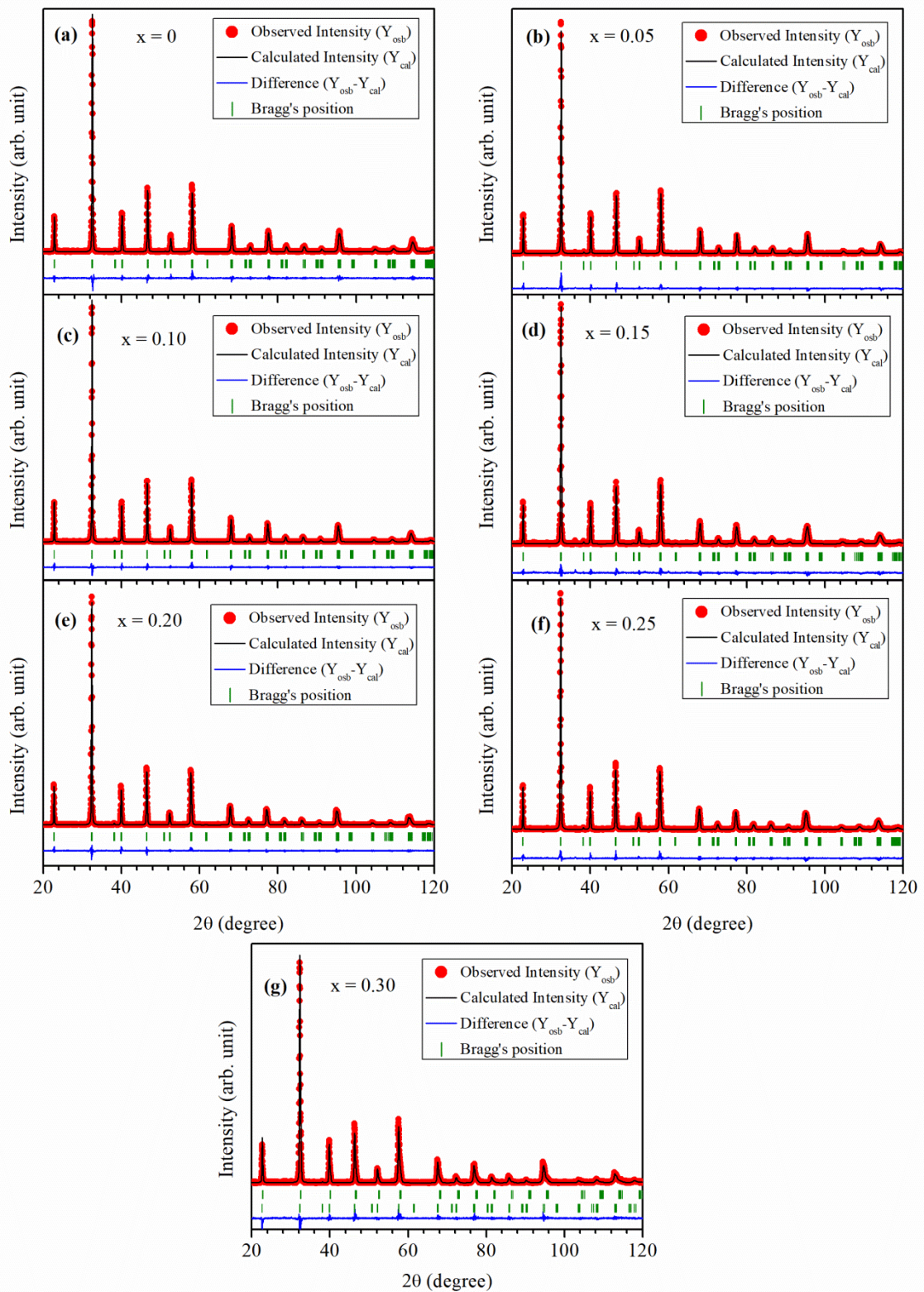**Figure 3.4:** Rietveld fits for the XRD patterns of $Nd_{0.7}Ba_{0.3}Mn_{1-x}Ti_xO_3$ compounds using orthorhombic *Imma* space group (a) x = 0, (b) 0.05, (c) 0.10, (d) 0.15, (e) 0.20, (f) 0.25 and coexistence of tetragonal *I4/mcm* and *P4mm* space groups (g) 0.30.

Fig. 3.5 shows the variation in lattice parameters and unit cell volume as a function of the doping concentration of Ti^{4+}-ion. This clearly shows that the values of lattice parameters and unit cell volume are increasing with increasing concentration of Ti^{4+}-ions and a structural phase transition close to the composition $x = 0.30$ from orthorhombic to tetragonal structures.

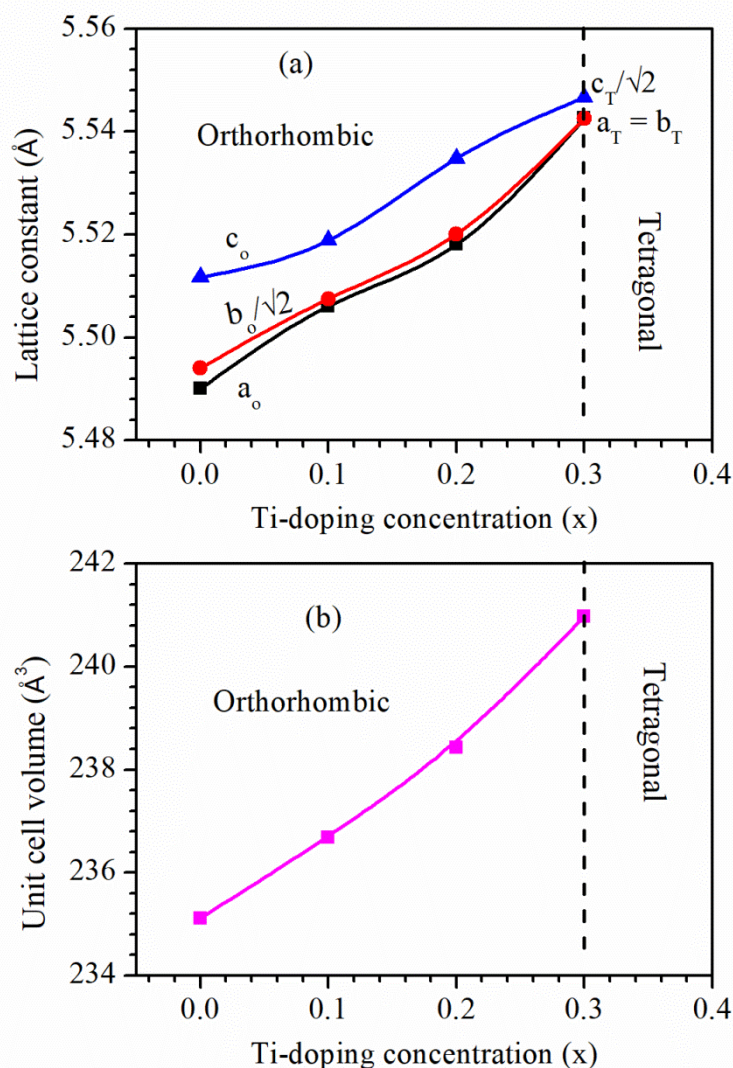**Figure 3.5:** Variation of (a) lattice parameters and (b) unit cell volume with Ti^{4+}-ions doping concentration (x) for $Nd_{0.7}Ba_{0.3}Mn_{1-x}Ti_xO_3$ with $0 \leq x \leq 0.30$. Here, a_o, b_o, and c_o correspond to the lattice parameters for orthorhombic structure and a_T, b_T, and c_T for tetragonal structure.

The ball and stick models (BSMs) for the unit cell of NBMTO manganites for x < 0.30 and x = 0.30 are drawn with the help of VESTA software using results of the CIF files obtained after Rietveld structure refinement. **Fig. 3.6** presents BSMs for the unit cell showing MnO_6 octahedra present. This figure clearly shows the tilting of the MnO_6 octahedra from their ideality for the orthorhombic Imma and tetragonal I4/mcm space groups due to the distorted structure.
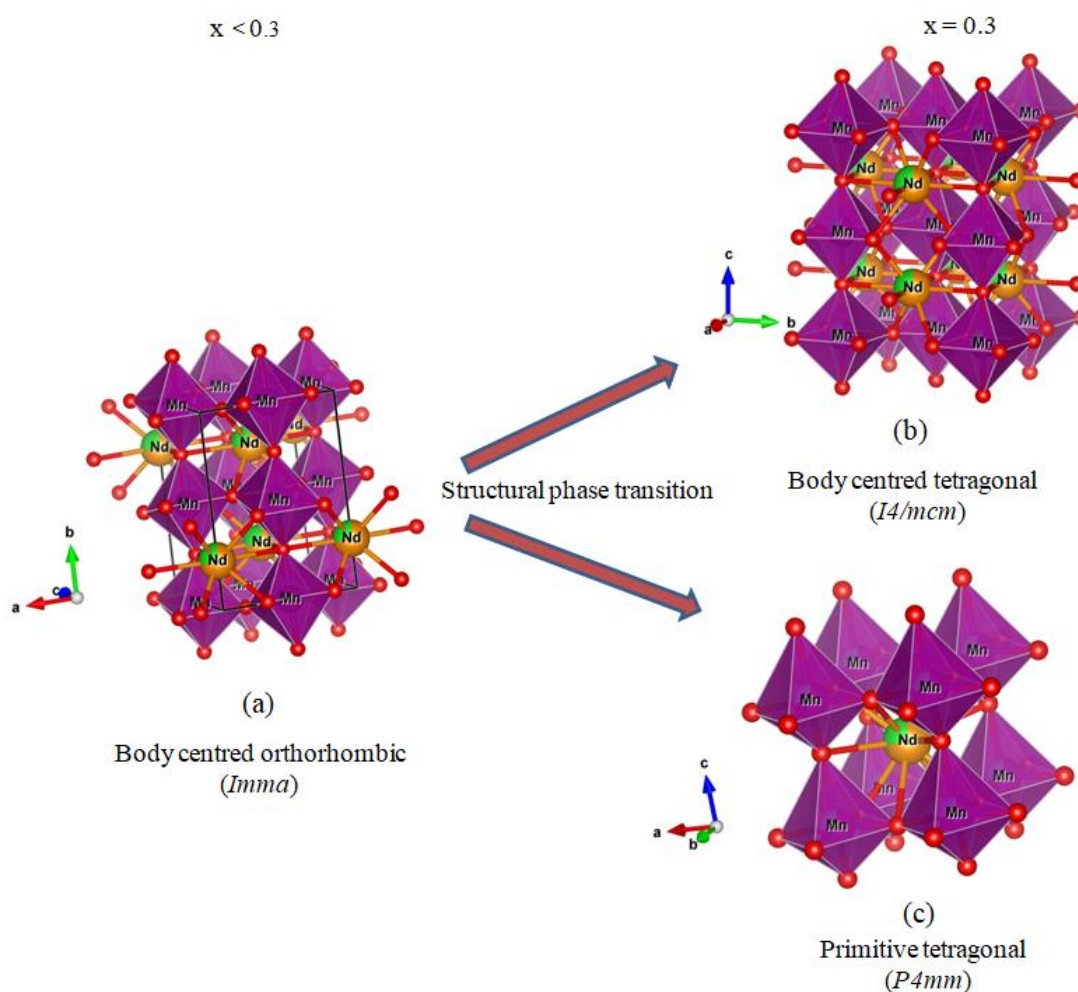

Figure 3.6: Ball and stick models for (a) *Imma* (x < 0.30), (b) *I4/mcm* (x = 0.30) and (c) *P4mm* (x = 0.30) space groups.

Table 3.2: Lattice parameters, unit cell volume, average bond-length and bond-angle and χ^2 for $Nd_{0.7}Ba_{0.3}Mn_{1-x}Ti_xO_3$ ($0 \leq x \leq 0.30$) manganites as determined from Rietveld structure refinement. Average crystallite size estimated using Debye-Scherrer formula (d_x) and particle size from SEM micrographs (d_{SEM}) are also listed.

Parameters	*Imma*						*I4/mcm*	*P4mm*
	x = 0	x = 0.05	x = 0.10	x = 0.15	x = 0.20	x = 0.25	x = 0.30	
$a(\text{Å})$	5.4900(6)	5.5178(3)	5.5061(5)	5.5292(5)	5.5181(4)	5.5339(6)	5.5426(5)	3.888(2)
$b(\text{Å})$	7.7697(9)	7.7784(8)	7.7888(6)	7.7804(10)	7.8066(6)	7.8149(7)	5.5426(5)	3.888(2)
$c(\text{Å})$	5.5117(5)	5.5005(4)	5.5189(5)	5.5064(9)	5.5348(2)	5.5152(6)	7.8442(5)	3.901(2)
$V(\text{Å}^3)$	235.11(4)	236.08(3)	236.68(4)	236.88(5)	238.43(3)	238.51(4)	242.20(4)	58.97(6)
$V_{dis}(\text{Å}^3)$	235.55	235.25	236.02	236.07	239.24	239.07	240.73	59.31
$d_{Mn-O}(\text{Å})$	1.958(3)	1.964(7)	1.964(4)	1.967(6)	1.967(5)	1.966(5)	1.974(6)	1.952(2)
$\theta_{Mn-O-Mn}(°)$	166.9(2)	165.0(3)	164.7(2)	165.0(4)	167.5(1)	167.5(2)	168.1(1)	174.7 (1)
d_x (nm)	46.01	68.78	53.42	47.41	46.27	52.85	39.41	80.27
d_{SEM} (nm)	375	460	540	555	560	650	435	
χ^2	1.48	1.54	1.46	1.41	1.32	1.34	1.48	

3.3.3. Magnetic Properties

3.3.3.1. Temperature Dependent Magnetization Studies

The temperature dependent magnetization M(T) curves of NBMTO with x = 0, 0.05, 0.10, 0.15, 0.20, 0.25 and 0.30 were measured in zero field cooled (ZFC) and field cooled (FC) conditions under the constant applied field. **Fig. 3.7**(a) shows variation in dc magnetic susceptibility as a function of temperature for NBMTO manganites. In higher temperature region (> 200 K), the value of magnetization is almost zero for all these samples. With lowering temperature, the magnetization increases slowly and below certain temperature, rises rapidly, reaches the maximum value and start decreasing on the further decrease of temperature. This suggests that all the samples undergo paramagnetic (PM) to ferromagnetic (FM) phase transition at characteristic Curie temperature T_C, determined by the temperature corresponding to peak appearing in dM_{ZFC}/dT vs. T curves as shown in **Fig. 3.7**(b) for x = 0, 0.05 and 0.10 [Ho et al.

(2017)]. The value of T_C decreases from 140 K for x = 0 to 39 K for x = 0.30. The doping of non-magnetic Ti^{4+}-ions at Mn-site weakens double exchange (DE) interaction which results reduction in T_C. The strength of DE interaction depends on the ratio of Mn^{4+}/Mn^{3+} in the manganites. This ratio decreases from 3/7 for x = 0.0 to 0 for x = 0.30. Thus, doping of both magnetic and non-magnetic ions on Mn-site in manganites reduces the strength of DE interaction causing decrease of Curie temperature [Zhu et al. (2006); Kim et al. (2005); Ho et al. (2016); Zhu et al. (2010); Dayal et al. (2015); Phan et al. (2015); Gasmi et al. (2009); Baazaoui et al. (2016); Bau et al. (2016); Ho et al. (2017)]. The experimentally observed values of T_C decrease exponentially with increasing doping concentration of Ti^{4+}-ions. The experimental value of T_C, was fitted using exponentially decaying function [$T_C = T_0 + T_1 \times exp(-x/t)$], where, T_0, T_1 and t are fitting parameters and x is the Ti-doping concentration, shows good agreement with the experiment data, as shown in **Fig. 3.7**(c). The value of fitting parameters are found to be $T_0 = 34.1(1)$ K, $T_1 = 106.2(2)$ K and t = 0.0765(4). Further, the bifurcation between ZFC and FC magnetization curves of the NBMTO manganite samples may be due to spin-glass or spin-glass cluster behaviour [Dayal et al. (2014); Zhu et al. (2006)]. **Fig. 3.7**(d) displays temperature dependence of irreversible magnetization M_{irr} (=M_{FC}-M_{ZFC}), which decreases with increasing concentration of Ti^{4+}-ion. It is clearly visualized from M vs. T curves that irreversible temperature (T_{irr}) is always higher than the temperature corresponding to the maxima in the magnetization (T_{max}) representing the occurrence of large-sized spin clusters which are ordered in the higher temperature region. For the samples with x ≤ 0.05, M_{ZFC} and M_{FC} show maxima in the low-temperature region at different temperatures (T_{max}) and M_{FC} decreases on further lowering temperature below T_{max}. However, for the doped samples with x > 0.05, M_{ZFC} and M_{FC} both exhibit maxima at the same temperature (T_{max}), but, M_{FC} first decreases and then increases on

further lowering of temperature below T_{max} as shown in the inset of **Fig. 3.7**(c). This shows that the spin glass nature of compounds with $x > 0.05$ is different from the compounds with $x \leq 0.05$. Furthermore, the samples with $x \leq 0.05$ clearly exhibit partial/full FM ordering of Nd-moment with Mn-moments below 40 K [Roy et al. (2008)].

In all the magnetization curves, we do not get any signature of the contribution from ferrimagnetic ordering of small impurity Mn_3O_4, which has Curie temperature T_C = 42 K [Dwight et al. (1960)]. The T_C of the NBMTO sample with $x = 0.25$ is same as that for Mn_3O_4. On the basis of the results for the NBMTO samples with $x = 0.05$ and 0.15 where no contribution of Mn_3O_4 in the magnetization is detectable, we conclude that Mn_3O_4 has no effective contribution in the magnetization of the NBMTO sample with $x = 0.25$ also. Hence, in the calculation of effective paramagnetic moment and saturation moment, we do not take account the contribution of Mn_3O_4 which is present in very small fraction (less than 2%).
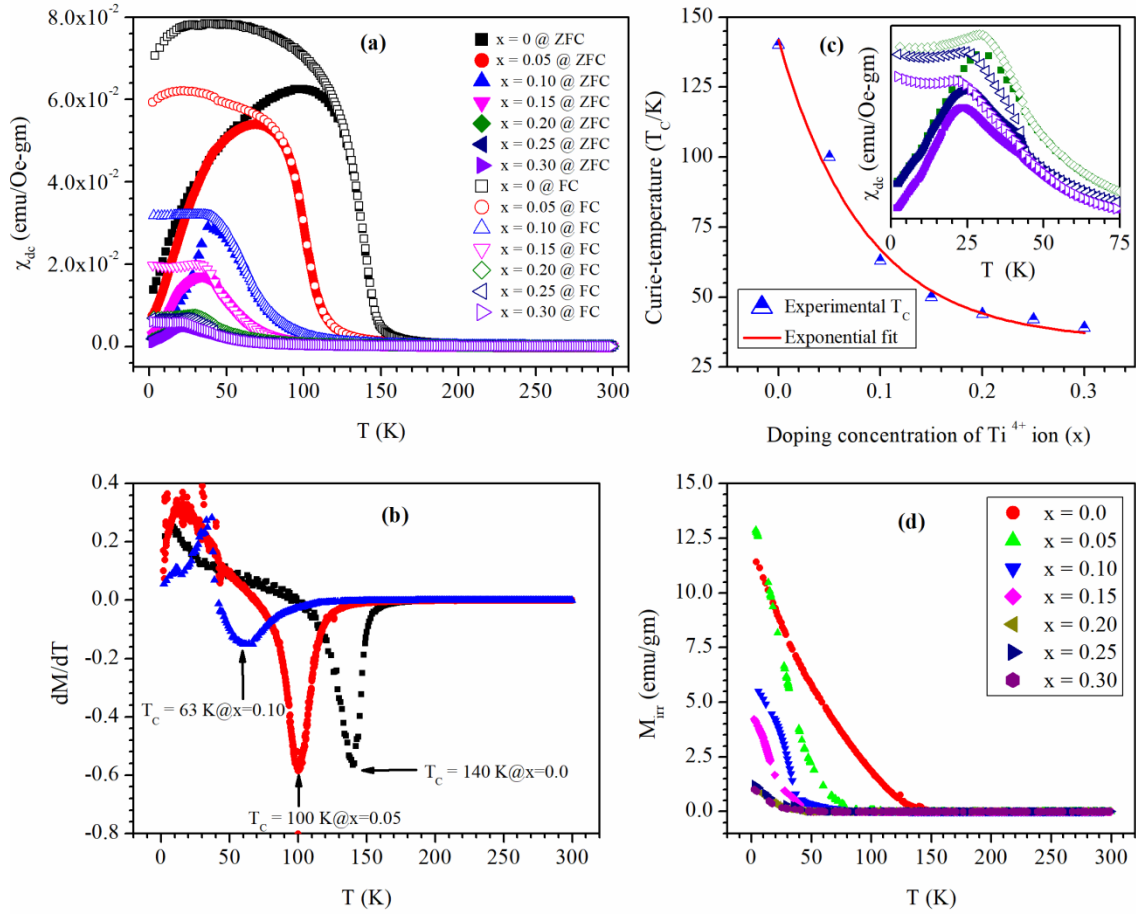
Figure 3.7: (a) Temperature dependence of χ_{ZFC} (close symbol) and χ_{FC} (open symbol) for $Nd_{0.7}Ba_{0.3}Mn_{1-x}Ti_xO_3$ compounds with $0 \leq x \leq 0.30$. (b) dM/dT curves as a function of T for x = 0, 0.05 and 0.10. (c) Exponential variation of T_C as a function of doping concentration of Ti^{4+}-ion. Inset shows low-temperature zoomed view of $\chi_{ZFC/FC}$ for x = 0.20, 0.25 & 0.30. (d) Temperature dependent variation in irreversible magnetization.

3.3.3.2. Temperature Dependent Inverse dc Susceptibility Studies

Fig. 3.8(a) shows the temperature dependent inverse molar susceptibility for NBMTO with x = 0.0, 0.05, 0.10, 0.15, 0.20, 0.25 and 0.30. In the high-temperature regime (T > T_C) molar susceptibility obeys the Curie-Weiss law: $\chi_m^{-1} = (T - \theta_{CW})/C$, where, C is Curie constant and θ_{CW} is Curie-Weiss temperature. A curve of χ_m^{-1} vs. T for each sample gives straight line in this temperature region. The value of Curie-Weiss temperature (θ_{CW}) was determined from the intercept of the straight line with the

temperature axis and the value of effective paramagnetic moment from the slope of the line. The value of θ_{CW} is found to be positive and larger than the value of T_C, which indicates that FM interactions are dominant in the higher temperature paramagnetic region [Hazzez et al. (2016)]. The experimental effective paramagnetic moment μ_{eff}^{exp} in units of Bohr magneton (μ_B) of the samples was calculated using Equation (3.2) expressed as:

$$\mu_{eff}^{exp} (\mu_B) = \sqrt{3k_B C/N_a \mu_B^2} = \sqrt{8C} \tag{3.2}$$

Here, k_B is Boltzmann constant, C is the inverse of the slope of the fitted straight line and N_a is Avogadro's number [Phong et al. (2017); Jemma et al. (2015); Kundu et al. (2013)]. The experimental value of effective paramagnetic moment was found to be 7.28, 6.88, 6.84, 6.82, 6.50, 5.82 and 5.22 μ_B for the NBMTO samples with x = 0, 0.05, 0.10, 0.15, 0.20, 0.25 and 0.30, respectively. **Fig. 3.8**(b) shows exponential variation of $\mu_{eff}^{exp} (\mu_B)$ with positive curvature as a function of Ti-doping concentration (x). The effective paramagnetic moment can be calculated as: $\mu_{eff}^{exp} (\mu_B) = \mu_0^{exp} + \mu_1^{exp} \times e^{-x/t}$, where, $\mu_0^{exp} = 6.884\,\mu_B, \mu_1^{exp} = -0.001\mu_B$ and t = 0.035. The $\mu_{eff}^{exp} (\mu_B)$ varies from 7.28 μ_B for x = 0 to 5.22 μ_B for x= 0.30. The values of θ_{CW} obtained from Curie-Weiss fit are greater than the value of T_C obtained from dM_{ZFC}/dT peak position, which may be attributed to the magnetic inhomogeneities resulting in short-range magnetic order slightly above T_C [Kundu et al. (2013)]. The theoretical value of effective paramagnetic moment in the units of Bohr magneton (μ_B) of all the samples was calculated using the relation [Phong et al. (2017); Kundu et al. (2013)] given by Equation (3.3):

$$\mu_{eff}^{theo} (\mu_B) = \sqrt{0.7\mu_{eff}^2(Nd^{3+}) + 0.7\mu_{eff}^2(Mn^{3+}) + (0.3-x)\mu_{eff}^2(Mn^{4+})} \tag{3.3}$$

With $\mu_{eff}^{theo}(Nd^{3+}) = 3.62\,\mu_B$, $\mu_{eff}^{theo}(Mn^{3+}) = 4.9\,\mu_B$ and $\mu_{eff}^{theo}(Mn^{4+}) = 3.87\,\mu_B$ [Phong et al. (2017); Phong et al. (2016a); Kossi et al. (2015); Hazzez et al. (2016);

Kundu et al. (2013)]. The value of μ_{eff}^{theo} (μ_B) decreases from 5.51 μ_B for x = 0 to 5.10 μ_B for x = 0.30. The experimental value of effective paramagnetic moment is greater than the theoretical value of effective paramagnetic moment which could be due to the presence of FM clusters in PM state [Hazzez et al. (2016)].
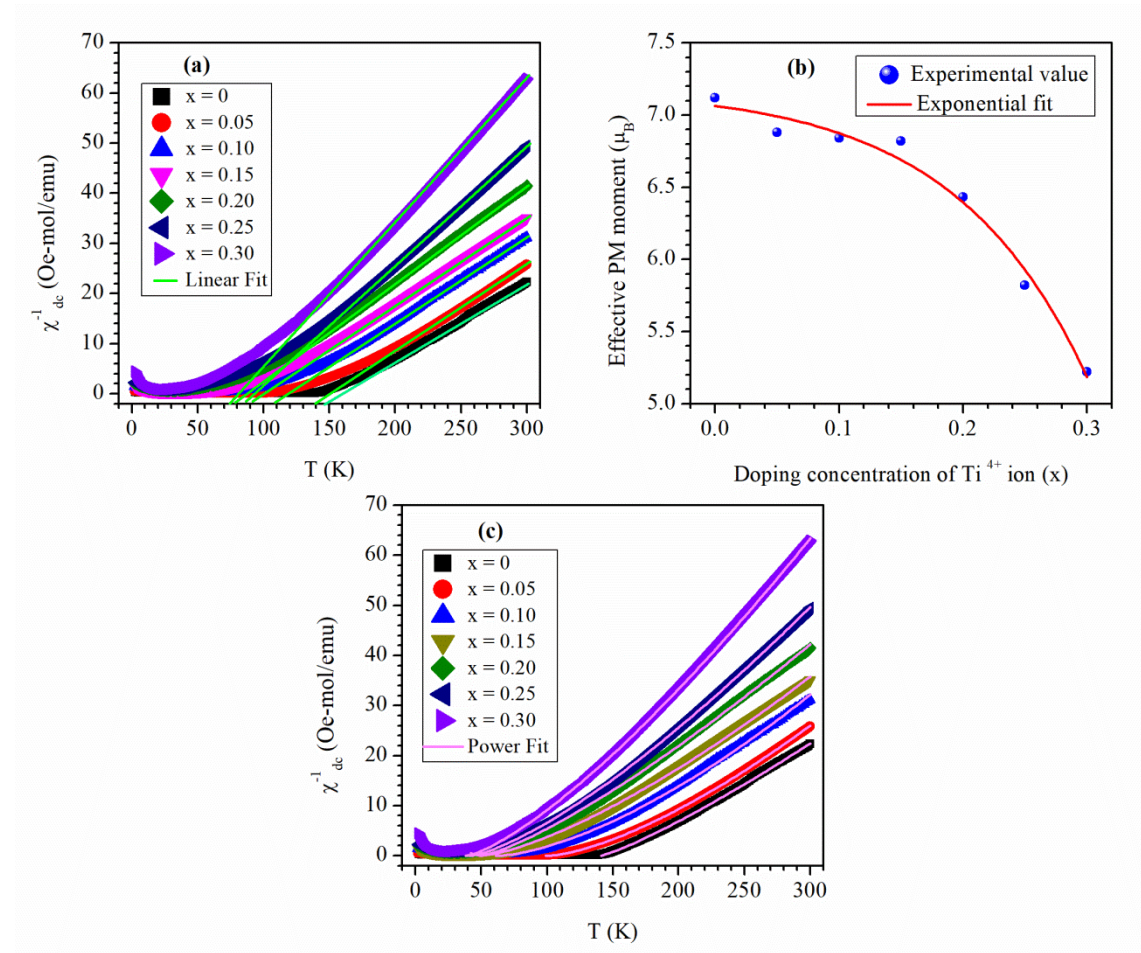

Figure 3.8: (a) and (c) Temperature dependent inverse dc susceptibility of NBMTO manganites with $0 \leq x \leq 0.30$. The dots indicate the experiment data while solid lines indicate the linear fit. (b) Variation of experimental value of μ_{eff}^{exp} (μ_B) as a function of Ti-doping content for NBMTO with $0 \leq x \leq 0.30$.

The critical exponent (γ) for magnetic susceptibility for each sample was calculated using Equation (3.4):

$$\chi_m^{-1} = A|T - T_C|^{\gamma} \tag{3.4}$$

Where, A is a proportionality constant and γ is the critical exponent for magnetic susceptibility [Chaikin et al. (2000)]. **Fig. 3.8**(c) shows experimental and fitted curves using above relation for inverse susceptibility. It is found that critical exponent of magnetic susceptibility decreases with increasing Ti-doping. The value of magnetic susceptibility critical exponents (γ) have been found to be 1.21, 1.49, 1.54, 1.40, 1.36, 1.35 and 1.33 for x = 0, 0.05, 0.10, 0.15, 0.20, 0.25 and 0.30, respectively. This suggests that the nature of magnetic interactions for the sample with x = 0 is close to as per 3D Ising model (γ = 1.241) and for the sample with x = 0.30 magnetic interaction is close to 3D Heisenberg model (γ = 1.336), while, the value of γ for other samples i.e., for x = 0.05, 0.10, 0.15, 0.20 and 0.25 is higher than that for 3D Heisenberg model. This may be attributed to the inhomogeneous nature of magnetic ordering in x = 0.05, 0.10, 0.15, 0.20 and 0.25 samples. In general, the value of γ is of the order 4/3 = 1.33 for three-dimensional systems where critical fluctuations are important [Chaikin et al. (2000); Baazaoui et al. (2016)].

Table 3.3: The magnetic parameters for $Nd_{0.7}Ba_{0.3}Mn_{1-x}Ti_xO_3$ manganites with $0 \leq x \leq 0.30$. The Curie temperature T_C, Curie-Weiss temperature θ_{CW}, Curie constant C, experimental effective paramagnetic moment [μ_{eff}^{exp} (μ_B)], theoretical effective paramagnetic [μ_{eff}^{theo} (μ_B)], critical exponent for magnetic susceptibility (γ) and AFM fraction present in the sample.

x	0	0.05	0.10	0.15	0.20	0.25	0.30
T_C (K)	140	100	63	50	42	42	39
θ_{CW} (K)	154.17	148.05	117.14	96.12	81.48	92.12	84.66
C(emu.K/Oe.mol)	6.62	5.92	5.85	5.81	5.28	4.23	3.40
μ_{eff}^{exp}(μ_B)	7.28	6.88	6.84	6.82	6.50	5.82	5.22
μ_{eff}^{theo}(μ_B)	5.51	5.45	5.38	5.31	5.24	5.17	5.10
Critical exp. (γ)	1.21	1.49	1.54	1.40	1.36	1.35	1.33
μ_{sat}^{theo}(μ_B)	3.70	3.55	3.40	3.25	3.10	2.95	2.80
μ_{sat}^{exp}(μ_B) @ 10 K	2.49	-	1.88	-	1.40	-	1.08
μ_{sat}^{exp}(μ_B) @ 5 K	-	3.06	-	1.84	-	1.28	-
AFM (%) @10 K	33	-	45	-	55	-	61
AFM (%) @5 K	-	14	-	43	-	57	-

3.3.3.3. Field Dependent Magnetization Studies

To further explore the nature of magnetic properties of the Ti-doped NBMTO samples, we performed field dependence of magnetization measurement M(H) at different temperatures. **Figs. 3.8**(a-c) show field dependent magnetization at 10 K for x = 0, 0.10, 0.20 & 0.30; at 5 K for 0.05, 0.15 & 0.25 and 50 K for 0.05, 0.15 & 0.25, respectively. The inset of **Figs. 3.8**(a-c) display low-field zoomed view of M(H) hysteresis curves.

In **Figs. 3.8**(a-c), for the sample with $0 \leq x \leq 0.10$ magnetization increases rapidly at low magnetic fields which resembles a ferromagnetic nature with long-range

FM ordering corresponding to the rotation of the magnetic domains. However, the magnetization increases slowly and continuously without saturation at higher fields, showing a coexistence of FM and AFM components [Liu (2015)]. For the sample with x = 0.25 (T_C = 42 K) the field dependent magnetization curve at 50 K shows finite hysteresis and non-linear variation of magnetization, resulting due to short-range FM ordering in PM state. The value of remnant magnetization (M_r) and coercive field (H_C) increases on going from high temperature (50 K) to low temperature (5 K) for x = 0.05, 0.15 and 0.25 and decreases with increasing doping concentration of Ti^{4+}-ion. As mentioned above, the introduction of Ti^{4+} ions replaces Mn^{4+} (Ar, $3d^3$) ions from the system causing lattice expansion. Since Ti^{4+}-ion is non-magnetic with empty $3d^0$ orbits, there is no possibility of FM interactions between Mn^{4+} and Ti^{4+} ions. Hence, doping of Ti^{4+} non-magnetic cations reduces Mn^{3+}-O^{2-}-Mn^{4+} double exchange (DE) interactions in the system which results in weakening of FM ordering and reduction of T_C.
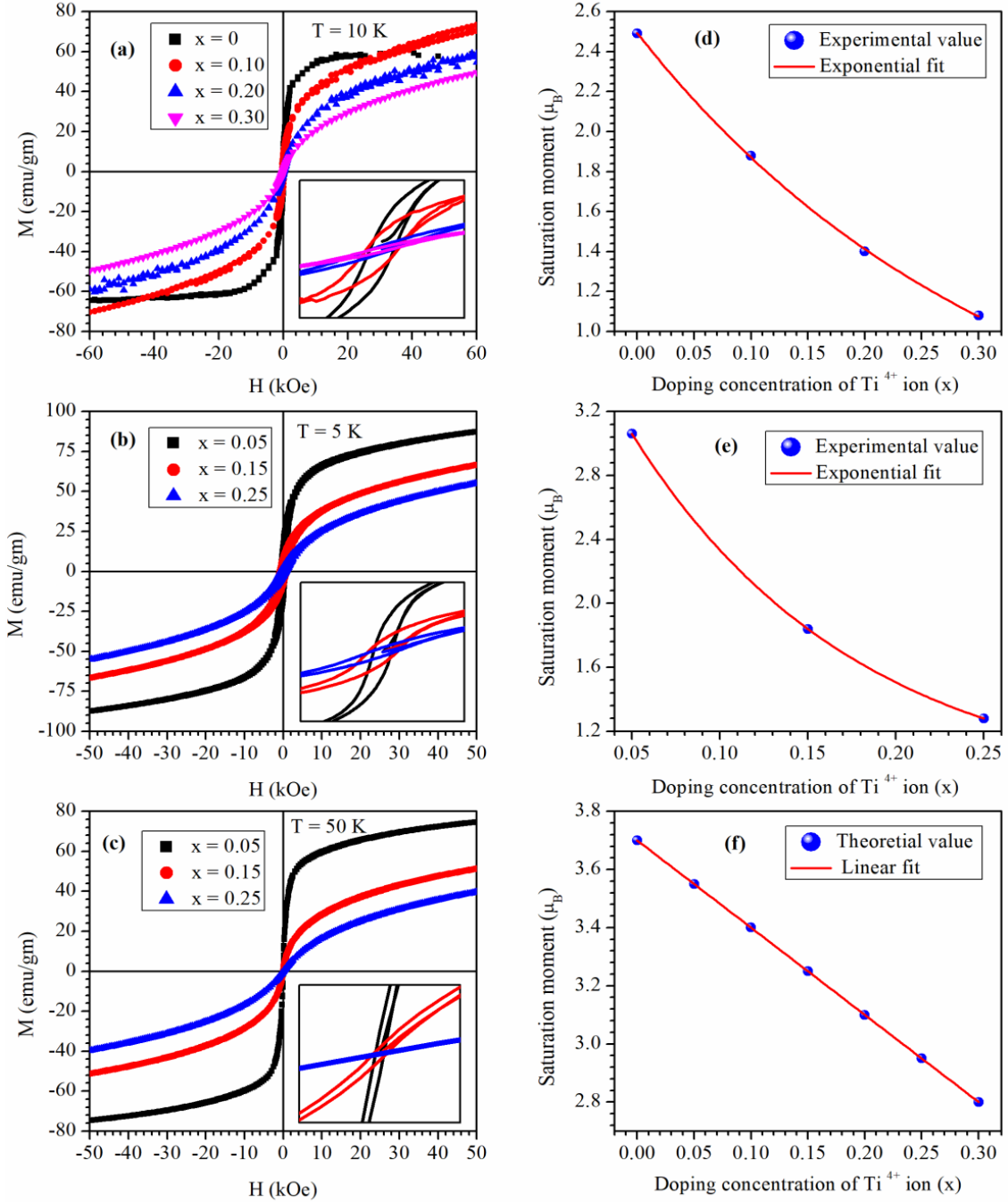
Figure 3.9: (a-c) Magnetic hysteresis curves for NBMTO manganites with $0 \leq x \leq 0.30$ at different temperatures. Inset shows low-field zoomed view of M(H) curves. Variation of (d-e) experimental and (f) theoretical saturation moments with doping concentration of Ti^{4+}-ion.

To further explore the magnetic behavior of the samples in low-temperature region, we estimated experimental values of saturation moment and compared with the theoretical values of spin only saturation moment. The experimental values of saturation moment in the unit of Bohr magneton were calculated using Equation (3.5):

$$\mu_{sat}^{exp}(\mu_B) = \frac{M_{sat}^{exp} M_m}{N_a \mu_B} \tag{3.5}$$

Where, M_m is the molecular weight of the sample, M_{sat}^{exp} is the experimental value of saturation magnetization, μ_B is Bohr magneton, and N_a is Avogadro's number. The value of M_{sat}^{exp} also denoted by M_s was determined by magnetization value obtained by extrapolating a straight line from higher magnetic field to zero magnetic field. The experimental values of saturation moment at 10 K were found to be 2.49, 1.88, 1.40 and 1.08 μ_B for the samples with x = 0, 0.10, 0.20 and 0.30, respectively, and at 5 K were found to be 3.06, 1.84 and 1.28 for x = 0.05, 0.15 and 0.25, respectively, which decreases exponentially with increasing doping concentration of Ti^{4+}-ion (x) as shown in **Figs. 3.9**(d-e), respectively. However, the theoretical spin only values of saturation moment were estimated considering full alignments of the spins of Mn^{3+} and Mn^{4+} ions taking dilution effect of Ti^{4+} ions using the equation: $\mu_{sat}^{theo}(\mu_B) = 0.7M_{Mn^{3+}} + (0.3-x)M_{Mn^{4+}} + xM_{Ti^{4+}} = 2\mu_B\left[0.7 \times \frac{4}{2} + (0.3-x) \times \frac{3}{2}\right]$, and are found to be 3.70, 3.55, 3.40, 3.25, 3.10, 2.95 and 2.80 μ_B for the samples with x = 0, 0.05, 0.10, 0.15, 0.20, 0.25 and 0.30, respectively. It decreases linearly with doping concentration of Ti^{4+}-ion as shown in **Fig. 3.9**(f). The inconsistent behavior between experimental and theoretical saturation moments reveals the inhomogeneity of the magnetic ordering. It is also found that theoretical values of saturation moment are greater than that of an experimental one, which suggests the existence of short-range AFM ordered component

within the FM ordering in the low temperatures regime. The presence of short-range AFM ordering increases with doping of Ti^{4+} ions as presented in **Table 3.3**.

Recently, Amaral et al. (2004) described the magnetocaloric effect in ferromagnetic systems of lanthanum manganites in terms of the Landau theory of phase transition and proposed that the magnetoelastic and magnetoelectronic couplings account for the temperature dependence of magnetic entropy change. Consequently, the Gibbs free energy is expressed by the relation: $G(T, M) = G_0 + \frac{1}{2}AM^2 + \frac{1}{4}BM^4 - MH$, where G_0 is temperature independent constant, while A and B are temperature dependent coefficients [Kossi et al. (2015)]. From the equilibrium condition near the Curie temperature, i.e., the minimization of energy, $\partial G/\partial M = 0$, the magnetic equation of state is obtained as $H/M = A + BM^2$ [Liu (2015)]. The nature of the magnetic phase transition in all the Ti-doped samples can be confirmed using the Banerjee criterion [Banerjee (1964)]. According to this criterion, the magnetic transition is of second order if all the isothermal M^2 vs. H/M curves have a positive slope. On the other hand, if some of the isothermal M^2 vs. H/M curves show a negative slope in some region, the transition is of first order [Ho et al. (2016); Banerjee (1964)]. **Fig. 3.10** displays the isothermal M^2 vs. H/M Arrott's plots for $Nd_{0.7}Ba_{0.3}Mn_{1-x}Ti_xO_3$ manganites for $0 \leq x \leq 0.30$. Furthermore, it is observed that the isothermal M^2 vs. H/M curves are not parallel to each other (for x = 0.05, 0.15 and 0.25) in high field region and deviate from the straight line. This indicates that the magnetization of the samples does not obey ideal mean field theory type behaviour ($\beta = 0.5$, $\gamma = 1$), as already discussed in the previous section. However, positive slope in the higher field region of the isothermal M^2 vs. H/M plots for all the samples and the negative slope in the low field region confirm that all the studied samples undergo the first order magnetic phase transition [Ho et al. (2016)]. Leal et al. (2007) reported that M^2 vs. H/M for $La_{2/3}Ca_{1/3}MnO_3$ manganite displays negative slope

in the high field region and positive slope in very low field regime, which shows first order phase transition around T_C. They also studied the effect of variance of the A-site ionic radii distribution σ^2 on the magnetic phase transition for the series of $[La_{1-x}Nd_x]_{2/3}[Ca_{1-y}Sr_y]_{1/3}MnO_3$ (LNCSMO) manganites and found that with increasing σ^2 up to a certain value, the order of magnetic phase transition changes from first order to second order. A similar behaviour was also observed in $La_{2/3}Ca_{1/3}MnO_3$ manganite with increasing measurement pressure [Leal et al. (2007)]. Further, the existence of spontaneous magnetization at 10 K of $M_0 = 56.61$ emu/gm for the parent sample (x = 0), $M_0 = 13.75$ emu/gm, $M_0 = 60.4$ emu/gm at 5 K for the sample with x = 0.10 and 59.2 emu/gm at 50 K for the sample with x = 0.05 suggests that the samples with x = 0, 0.05 & 0.10 are exhibiting long-range FM ordering. However, the isothermal M^2 vs. H/M plots for the samples with x = 0.15, 0.20, 0.25 and 0.30 do not exhibit spontaneous magnetization, which indicates the existence of long range AFM ordering at low temperatures [Kumar et al. (2019)]. **Table 3.3** presents various magnetic parameters deduced from experimental and theoretical calculations.
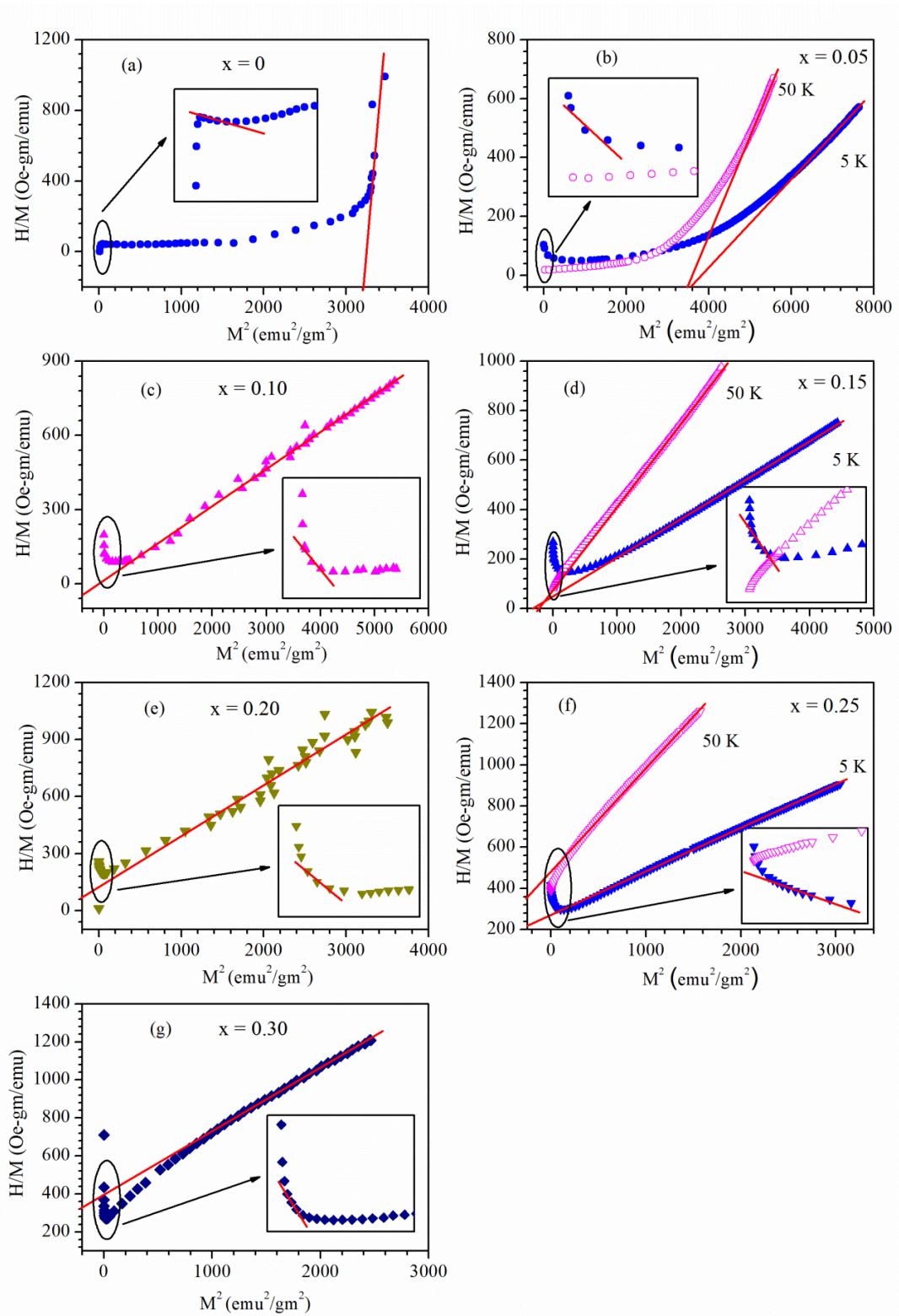
Figure 3.10: Isothermal Arrott's plots (M^2 vs. H/M) for $Nd_{0.7}Ba_{0.3}Mn_{1-x}Ti_xO_3$ manganites with (a) x = 0, (b) x = 0.05, (c) x = 0.10, (d) x = 0.15, (e) x = 0.20, (f) x = 0.25 and   (g) x = 0.30.

3.3.3.4. Temperature Dependent ac Susceptibility Studies

We performed a qualitative analysis of temperature-dependent ac-susceptibility for $Nd_{0.7}Ba_{0.3}Mn_{1-x}Ti_xO_3$ ($0 \leq x \leq 0.30$) manganites. In **Fig. 3.11** the temperature dependent ac-susceptibility is plotted for the samples with x = 0, 0.10, 0.20 and 0.30 measured at two frequencies 100 and 700 Hz in the temperature range of 2 to 300 K. In **Fig. 3.11** the left channel shows the in-phase component (real part) $\chi'(T)$ of the ac-susceptibility and the right channel presents out of phase component (imaginary part) $\chi''(T)$ of the ac-susceptibility. The low-temperature behaviour of $\chi'(T)$ is qualitatively the same for all the samples. Below 150 K, $\chi'(T)$ shows a broad maximum which slightly decreases in amplitude at higher frequencies for the sample with x = 0. For the parent sample (x = 0), the maxima peak in the real part and imaginary part of ac-susceptibility shows frequency independent change as observed by the earlier authors along with ordering of Nd^{3+} ions (T_{Nd}) below 20 K [Roy et al. (2008)]. For doped samples (x > 0) the maxima peak shifted towards higher temperature side with increasing frequencies. It is well identified that $\chi'(T)$ in paramagnetic regime increases with decreasing temperature while for ferromagnetic regime below T_C, $\chi'(T)$ decreases with decreasing temperature. The peak corresponding to maxima in the $\chi'(T)$ may be identified as spin glass freezing temperature (T_f) [Sahoo et al. (2016)]. Additionally, for the samples with x = 0.20 and 0.30 a small shoulder appears before T_f as indicated in $\chi'(T)$ of **Figs. 3.11**(c-d).

Further, the qualitative behavior of the $\chi''(T)$ for the sample with x = 0 is also similar to the earlier report [Roy et al. (2008)]. The $\chi''(T)$ for the sample with x = 0.10 displays a sharp narrow peak at freezing temperature T_f along with another peak at a low temperature corresponding to ordering of Nd^{3+} ions (T_{Nd}). For the samples with x = 0.20 and 0.30, the behaviour of $\chi''(T)$ is different from the other samples. When the

temperature is lowered down from PM state in these systems, $\chi''(T)$ a frequency independent local maxima appears at Curie temperature (T_C) corresponding to PM to FM phase transition. On further lowering the temperature, $\chi''(T)$ reaches maxima at T_f and then $\chi''(T)$ decreases sharply and attain local maxima T_{Nd}. This is usually connected to the existence of a reentrant spin glass (RSG) phase in these samples [Kameli et al. (2009); Pekala et al. (2006); Khan et al. (2007)]. The reentrant behavior has been found in various type of disordered magnetic materials wherein there is a competition between long-range FM ordering and spin-glass ordering. In such kind of systems, there is a majority of FM ordering between the individual spins and enough number of AFM ordering for creating considerable frustration in the system [Kameli et al. (2009)]. The general features of these two samples are the same alike reentrant spin glass (RSG).
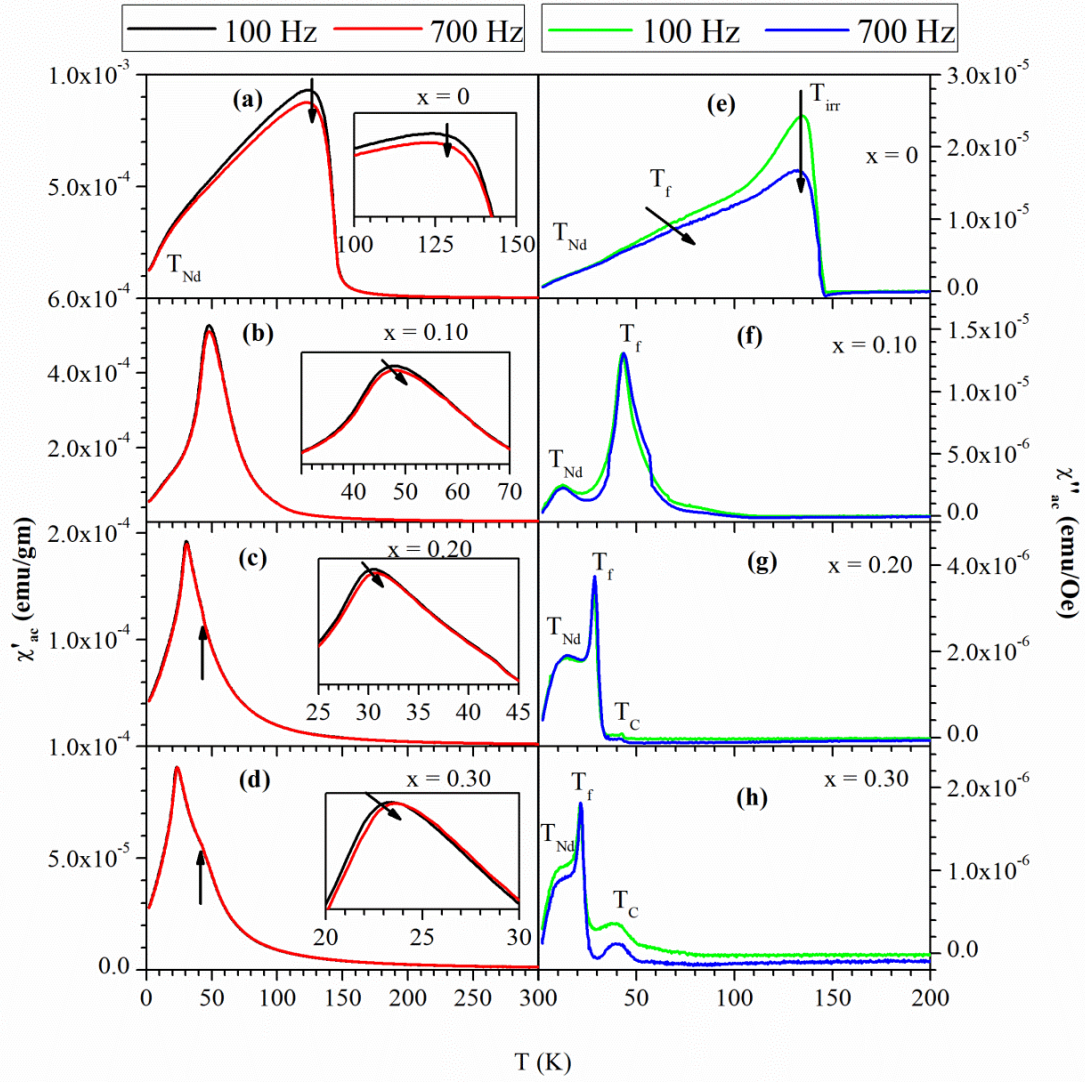
Figure 3.11: Temperature dependence of (a-d) real component $\chi'(T)$ and (e-h) imaginary part of ac-susceptibility $\chi''(T)$ for $Nd_{0.7}Ba_{0.3}Mn_{1-x}Ti_xO_3$ compounds with x = 0, 0.10, 0.20 and 0.30 measured during cooling for ac magnetic field amplitude at different frequencies. Insets of the left channel show the low-temperature view of real part $\chi'(T)$ of ac-susceptibility.

3.4. Conclusions

In summary, phase pure $Nd_{0.7}Ba_{0.3}Mn_{1-x}Ti_xO_3$ perovskites manganites with nominal compositions ($0 \leq x \leq 0.30$) were synthesized by combustion synthesis method followed by the calcination at 1200°C for 6 hrs. The effect of doping of Ti^{4+}-ion on structural and magnetic behaviours of these samples were examined by X-ray diffraction, scanning electron microscopy, energy dispersive X-ray spectroscopy, and magnetization measurements as a function of temperature and magnetic field. The Rietveld analysis of XRD data reveals that the manganites with compositions $x < 0.30$, crystallized into single phase orthorhombic structure with *Imma* space group, while, for the composition with $x = 0.30$ two phases of tetragonal structure with *I4/mcm* and *P4mm* space groups coexist. This shows a structural phase transition from orthorhombic structure to tetragonal structure in the vicinity of the composition $x \sim 0.3$. The unit cell volume for *Imma* space group increases from 235.10(5) $Å^3$ for $x = 0$ to 238.51(4) $Å^3$ for $x = 0.25$ with increasing doping concentration of Ti^{4+}-ion due to replacement of Mn^{4+}-ions by Ti^{4+}-ions. The temperature dependent magnetization measurement reveals that all samples exhibit PM to FM phase transition at Curie-temperature T_C. The value of T_C reduces exponentially from 140 K for $x = 0$ to 39 K for $x = 0.30$ with increasing doping content of Ti^{4+}-ion. The magnetic saturation is not reached even after the application of a magnetic field up to 60 kOe which can be related to a threshold in the diminution of Mn^{4+}/Mn^{3+} ratio. The decrease in T_C with Ti^{4+} doping is connected with the weakening of double exchange FM interaction and strengthening of the superexchange AFM interaction resulting due to the reduction of the Mn^{4+}/Mn^{3+} ratio. The field dependent magnetization M(H) shows the co-existence of two magnetic ordering FM and AFM. The bifurcation between ZFC and FC magnetization measurements indicates the possible existence of a spin glass cluster. Analysis of the isothermal M^2 vs. H/M

Arrott's plots exhibits that all samples show first order magnetic transition irrespective of Ti-doping. Temperature-dependent ac-susceptibility measurement confirms the spin glass cluster nature. The ac-susceptibility measurements study reveals that on Ti-doping systems undergo from one type of spin glass character to a different kind of spin glass nature.